



1 **Distinguishing between early and late covering crops in the land surface model**

2 **Noah-MP: Impact on simulated surface energy fluxes and temperature**

3

4 Kristina Bohm^{ab}, Joachim Ingwersen^b, Josipa Milovac^c, Thilo Streck^b

5

6

7 ^a previously published under the name Kristina Imukova

8 ^b Institute of Soil Science and Land Evaluation, Department of Biogeophysics, University of
9 Hohenheim, 70593 Stuttgart, Germany

10 ^c Institute of Physics and Meteorology, University of Hohenheim, 70593 Stuttgart, Germany

11

12

Corresponding author: Kristina Bohm

E-Mail: imukovaks@gmail.com



13 Abstract

14 Land surface models are essential parts of climate and weather models. The widely used Noah-
15 MP land surface model requires information on the leaf area index (LAI) and green vegetation
16 fraction (GVF) as key inputs of its evapotranspiration scheme. The model aggregates all
17 agricultural areas into a land use class termed “Cropland and Pasture”. In a previous study we
18 showed that, on a regional scale, GVF has a bimodal distribution formed by two crop groups
19 differing in phenology and growth dynamics: early covering crops (ECC, ex.: winter wheat,
20 winter rapeseed, winter barley) and late covering crops (LCC, ex.: corn, silage maize, sugar
21 beet). That result can be generalized for Central Europe. The present study quantifies the effect
22 of splitting the land use class “Cropland and Pasture” of Noah-MP into ECC and LCC on surface
23 energy fluxes and temperature. We further studied the influence of increasing the LCC share,
24 which in the study area (the Kraichgau region, southwest Germany) is mainly the result of
25 heavily subsidized biomass production, on energy partitioning at the land surface. We used the
26 GVF dynamics derived from high-resolution (5 m x 5 m) RapidEye satellite data and measured
27 LAI data for the simulations. Our results confirm that GVF and LAI strongly influence the
28 partitioning of surface energy fluxes, resulting in pronounced differences between ECC and LCC
29 simulations. Splitting up the generic crop into ECC and LCC had the strongest effect on land
30 surface exchange processes in July-August. During this period, ECC are at the senescence
31 growth stage or already harvested, while LCC have a well-developed, ground-covering canopy.
32 The generic crop resulted in humid bias, i.e. an increase of evapotranspiration by $+0.5 \text{ mm d}^{-1}$
33 (LE: $1.3 \text{ MJ m}^{-2}\text{d}^{-1}$), decrease of H by $1.2 \text{ MJ m}^{-2}\text{d}^{-1}$ and decrease of surface temperature by –
34 1°C . The bias increased as the shares of ECC and LCC became similar. The observed differences
35 will impact the simulations of processes in the planetary boundary layer. Increasing the LCC
36 share from 28 to 38% in the Kraichgau region led to a decrease of LE and a heating up of the
37 land surface in the early growing season. Over the second part of the season, LE increased and
38 the land surface cooled down by up to 1°C .

39



40 **1 Introduction**

41 Within weather and climate models, land surface exchange processes are simulated by so-called
42 land surface models (LSMs). The main role of an LSM is to partition net radiation at the land
43 surface into sensible heat (H), latent heat (LE) and ground heat (G) fluxes and to determine the
44 land surface temperature. Surface energy partitioning has a significant influence on the evolution
45 of the Atmospheric Boundary Layer (ABL). ABL evolution strongly influences the initiation of
46 convection, cloud formation, and ultimately the location and strength of precipitation (Crawford
47 et al. 2001, Koster et al. 2006, Santanello Jr. et al. 2013, van Heerwaarden et al. 2009, Milovac et
48 al. 2016).

49

50 The surface energy partitioning depends on the physical and physiological properties of the land
51 surface (Raddatz 2007). In LSMs, the earth's surface is subdivided into different land use classes,
52 among them cropland. Physiological state variables of crops such as green vegetation fraction
53 (GVF) and leaf area index (LAI) vary significantly throughout the growing season. This alters the
54 biophysical parameters surface albedo, bulk canopy conductance, and roughness length, leading
55 to significant changes in surface energy fluxes (Crawford et al. 2001, Ghilain et al. 2012,
56 Tsvetsinskaya et al. 2001a, Wizemann et al. 2014). In many parts of the world, cropland covers a
57 considerable part of the simulation domain. Therefore, accurately simulating the seasonal
58 variability of surface energy fluxes highly depends on an adequate representation of plant growth
59 dynamics.

60

61 One of the widely used LSMs is Noah-MP. It is usually coupled with the Weather Research and
62 Forecasting (WRF) model, which is intended for use from the large eddy simulation (LES) scale
63 up to the global scale. Within each grid cell, Noah-MP computes net longwave radiation as well
64 as LE, H and G separately for the bare soil and the vegetated tile, whereas short-wave radiation is
65 computed over the entire grid cell (semi-tile approach; Lhomme and Chehbouni 1999, Niu et al.
66 2011). Noah-MP collects agricultural areas into only general land use classes such as “Dryland
67 Cropland and Pasture”, “Irrigated Cropland and Pasture” or “Mixed Dryland/Irrigated Cropland
68 and Pasture” etc.. Vegetation dynamics and its seasonal development are described in the Noah-
69 MP model by the plant variables GVF and LAI. The surface energy fluxes critically depend on
70 accurately representing GVF and LAI dynamics (Chen and Xie 2011, Crawford et al. 2001,



71 Refslund et al. 2014). In Noah-MP, GVF and LAI are fixed quantities: they do not depend on the
72 weather conditions during a simulation. GVF is defined as the grid-cell fraction covered by a green
73 canopy (Gutman and Ignatov 1998). It is a function of the upper canopy (Rundquist 2002) and
74 represents the horizontal density of vegetation in each grid cell (Gutman and Ignatov 1998). LAI
75 represents the vertical density of the canopy. Certain biophysical parameters in Noah-MP such as
76 surface albedo, roughness and emissivity are considered linear functions of LAI.

77

78 By default, Noah-MP derives GVF values from the normalized difference vegetation index
79 (NDVI) obtained from the NESDIS/NOAA satellite. These data have a resolution of 15 km ×
80 15 km. Due to the mixing of croplands, forest and urban areas, the overall GVF is often positively
81 biased. Moreover, as shown by Imukova et al. (2015), seasonal GVF data are strongly smoothed
82 compared to the actual GVF dynamics. Milovac et al. (2016) and Nielsen et al. (2013) found that
83 the GVF grid data used in Noah-MP LSM are outdated and stated that these should be updated
84 given their importance for ABL evolution.

85

86 In a previous study, we derived GVF data with a resolution of 5 m x 5 m (Imukova et al. 2015) for
87 a region in southwest Germany (Kraichgau) using RapidEye satellite data. On the regional scale,
88 GVF shows a bimodal distribution mirroring the different phenology of crops. Crops could be
89 grouped into two classes. Early covering crops (ECC), such as winter wheat, winter rape, winter
90 barley and spring barley, develop early in spring, achieve maximum GVF usually between late
91 May and mid-June, and become senescent in July. Late covering crops (LCC), such as corn, silage
92 maize, and sugar beet, are drilled in spring and develop maximum ground-covering canopy from
93 July to August. They are still green in September, when the ECC are already harvested. The
94 dynamics of ECC and LCC vary to some degree from season to season and from region to region.

95

96 The shares of ECC and LCC may change over time, often reflecting economic decisions that may
97 depend on policy interventions. In Germany, a substantial change in these shares was introduced
98 by subsidizing biogas production. In 2005, 1.7 million ha of maize were cultivated in Germany.
99 Only 70,000 ha of this area were cropped with silage maize for biogas production (SRU Special
100 Report 2007). In 2009, the area cropped with maize for biogas production had increased to about



101 500,000 ha, while the total maize area remained almost constant (Huyghe et al. 2014). In 2012,
102 the total acreage of maize had increased to 2.57 million ha with 0.9 million ha intended for biogas
103 plants. The increase occurred mainly at the expense of grassland. Since then, the total maize crop
104 area has remained almost constant: 2.6 million ha in 2018 (Fachagentur Nachwachsende Rohstoffe
105 e. V. 2019). From 2005 to 2018, the maize area in Germany increased by about 53%.

106

107 The objectives of the present study were 1) to elucidate the extent to which surface energy fluxes
108 simulated with Noah-MP are affected by aggregating early and late covering crops into one generic
109 cropland class, and 2) to quantify the effect of a land use change, driven by the expansion of maize
110 cropping as a response to the increasing demand for biogas plants, on energy partitioning and
111 surface temperature in the Kraichgau region (southwest Germany).

112

113 **2 Materials and methods**

114 **2.1 Study site and weather data measurements**

115 Noah-MP simulations were performed for the Kraichgau region, which covers about 1500 km².
116 Mean annual temperature ranges between 9-10° C and annual precipitation between 730 and 830
117 mm. The Neckar and Enz rivers form the borders to the east. To the north and south, the region is
118 bounded by the low mountain ranges Odenwald and Black Forest. In the west, it adjoins the Upper
119 Rhine Plain (Oberrheinisches Tiefland). Kraichgau has a gently sloping landscape with elevations
120 between 100 and 400 m above sea level (a.s.l.). Soils predominantly formed from loess material.
121 The region is intensively used for agriculture: around 46 % of the total area is used for crop
122 production. Winter wheat, winter rapeseed, spring barley, corn, silage maize and sugar beet are the
123 predominant crops.

124

125 Weather data used to force the Noah-MP model were acquired at an agricultural field (EC1, 14 ha)
126 belonging to the farm “Katharinentalerhof”. The field is located north of the city of Pforzheim
127 (48.92°N, 8.70°E). The terrain is flat (elevation a.s.l.: 319 m). The predominant wind direction is
128 south-west. The study site has been described in detail in several studies (Imukova et al. 2015,
129 Ingwersen et al. 2011, Wizemann et al. 2014).



130

131 An Eddy Covariance (EC) station was operated in the center of the EC1 field. Wind speed and
132 wind direction were measured with a 3D sonic anemometer (CSAT3, Campbell Scientific, UK)
133 installed at a height of 3.10 m (2012). Downwelling longwave and downwelling shortwave
134 radiation were measured with a NR01 4-component sensor (NR01, Hukseflux Thermal Sensors,
135 The Netherlands). Air temperature and humidity were measured in 2 m height (HMP45C, Vaisala
136 Inc., USA). All sensors recorded data in 30-min intervals. Rainfall was measured using a tipping
137 bucket (resolution: 0.2 mm per tip) rain gauge (ARG100, Campbell Scientific Ltd., UK). For
138 further details about instrumentation and data processing see Wizemann et al. (2014).

139

140 **2.2 The Noah-MP v1.1 land surface model**

141 **2.2.1 Model parameterization**

142 Multi-physics options of Noah-MP were set as shown in the Table 1. For the simulation we used
143 the USGS land use dataset. The vegetation type index was set to 2 (Dryland cropland and
144 Pasture) and soil type index to 4 (Silt loam). The model was forced with half-hourly weather data
145 (wind speed, wind direction, temperature, humidity, pressure, precipitation, downwelling
146 longwave and shortwave radiation) measured at EC1 from 2011 to 2013. Simulations were
147 initialized with a spin up period of one year (2011) and run with a time step of 1800 seconds.



148 **Table 1.** Setting of the multi-physics options used in the Noah-MP simulation.

| Multi-physics option | Setting |
|--|---|
| Vegetation model | opt_dveg = 1: prescribed [table LAI, shdfac=FVEG] |
| Canopy stomatal resistance | opt_crs = 2: Jarvis |
| Soil moisture factor for stomatal resistance | opt_btr = 1: Noah |
| Runoff and groundwater model | opt_run = 1: SIMGM |
| Surface layer drag coefficient (CH & CM) | opt_sfc = 1: based on Monin-Obukhov similarity theory |
| Supercooled liquid water | opt_frz = 1: NY06 |
| Frozen soil permeability | opt_inf = 1: NY06 |
| Radiation transfer | opt_rad = 3: gap=1—Fveg |
| snow surface albedo | opt_alb = 2: CLASS |
| rainfall & snowfall | opt_snf = 1: Jordan91 |
| lower boundary of soil temperature | opt_tbot = 2: Noah |
| snow/soil temperature time scheme | opt_stc = 1: Semi-implicit |

149

150

151 **2.2.2 GVF dynamics**

152 The GVF data required by the Noah-MP model were derived from high-resolution (5 m x 5 m)
 153 RapidEye satellite data. As described by Imukova et al. (2015) the GVF data were calculated from
 154 the Normalized Difference Vegetation Index (NDVI) computed from the red and near-infrared
 155 bands of the satellite images. The relationship between GVF and NDVI was established by linear
 156 regression using ground truth measurements. GVF maps were derived in a monthly resolution.



157 **Table 2.** GVF dynamics of early covering crops (ECC) and late covering crops (LCC) in 2012 and 2013
 158 in the Kraichgau region, southwest Germany as well as the GVF dynamics of the generic crop.

| GVF | | 15 Apr | 15 May | 15 Jun | 15 Jul | 15 Aug | 15 Sep |
|-------------------------------------|-----|----------------|-------------|-------------------|-------------|-------------------|-------------|
| GVF 2012 | ECC | - ^b | 0.74 | 0.83 | 0.37 | 0.01 ^c | 0.01 |
| | LCC | - ^b | 0.01 | 0.35 | 0.74 | 0.69 ^c | 0.56 |
| GVF 2013 | ECC | 0.54 | 0.80 | 0.57 ^c | 0.29 | 0.01 | 0.01 |
| | LCC | 0.01 | 0.06 | 0.37 ^c | 0.69 | 0.74 | 0.75 |
| Mean GVF | ECC | 0.54 | 0.77 | 0.70 | 0.33 | 0.01 | 0.01 |
| | LCC | 0.01 | 0.04 | 0.36 | 0.72 | 0.72 | 0.66 |
| Generic crop GVF^a | | 0.39 | 0.57 | 0.60 | 0.44 | 0.21 | 0.19 |

^a Weighted mean GVF calculated based on fractions of ECC (72%) and LCC (28%) in Kraichgau

^b No RapidEye scenes were available for April

^c No RapidEye scenes were available for these months, GVF values were derived by linear interpolation between adjacent months

159

160 Table 2 shows the observed and mean GVF dynamics of ECC and LCC over the growing seasons
 161 2012 and 2013 as well as the GVF dynamics of the generic crop. The GVF values on the 15th day
 162 of each month, as required by Noah-MP model, were calculated by linearly interpolating the
 163 monthly values derived from the GVF maps. A generic GVF dynamics was calculated as the
 164 weighted mean of ECC and LCC from 2012 and 2013. The areal distribution of ECC and LCC
 165 was determined from the GVF maps of May. All pixels with a GVF value below 0.5 were counted
 166 as LCC, whereas pixels with values above that threshold were assigned to ECC. The estimated
 167 areal distribution of ECC and LCC was 72% and 28%, respectively. These results correspond well
 168 with data of the Statistisches Landesamt Baden-Württemberg (<http://www.statistik.baden-wuerttemberg.de/>).

170

171 2.2.3 LAI dynamics

172 Noah-MP requires prescribed LAI data for each month. Data were derived from field
 173 measurements. LAI was measured biweekly using a LAI-2000 Plant Canopy Analyzer (LI-COR
 174 Biosciences Inc., USA). In 2012 and 2013, LAI of the crops was measured on five permanently
 175 marked plots of 1 m² on three different fields. Detailed information about the study plots can be
 176 found in Imukova et al. (2015). In 2009-2011, LAI and the phenological development of the crops



177 were measured on five permanently marked plots of 4 m² in the same three fields. The growth
 178 stages of crops were determined using the BBCH scale (Meier et al. 2009). More details on the
 179 measurements can be found in Ingwersen et al. (2011) and Ingwersen et al. (2015). Table 3 shows
 180 measured and mean LAI dynamics as well as generic LAI dynamics estimated considering shares
 181 of ECC (72%) and LCC (28%) in the study region. LAI dynamics of winter wheat and winter rape
 182 were assigned to ECC, those of maize to LCC. Mean LAI dynamic of ECC was estimated based
 183 on the measurements conducted in winter wheat and winter rape stands during the 2012 and 2013
 184 growing seasons. Since LAI data were not available for maize in 2013, the mean LAI dynamic of
 185 LCC were assessed using field data from the same fields collected in 2009-2012.

186 **Table 3.** LAI dynamics of early covering crops (ECC) and late covering crops (LCC) in 2012 and 2013 in
 187 the Kraichgau region, southwest Germany, as well as the LAI dynamics of the generic crop.

| Green LAI | | 15 Apr | 15 May | 15 Jun | 15 Jul | 15 Aug | 15 Sep |
|-------------------------------------|------------------|------------|------------|------------|------------|------------|------------|
| LAI 2012 | ECC | 2.4 | 4.4 | 4.6 | 0.0 | 0.0 | 0.0 |
| | LCC | 0.0 | 0.1 | 0.9 | 3.2 | 5.0 | 3.7 |
| LAI 2013 | ECC | 1.7 | 4.2 | 4.3 | 0.0 | 0.0 | 0.0 |
| | LCC ^b | - | - | - | - | - | - |
| Mean LAI | ECC | 2.1 | 4.3 | 4.5 | 0.0 | 0.0 | 0.0 |
| | LCC ^c | 0.0 | 0.1 | 0.9 | 3.1 | 4.5 | 3.8 |
| Generic crop LAI^a | | 1.5 | 3.1 | 3.5 | 0.9 | 1.3 | 1.1 |

^a Areal weighted average LAI calculated taking into account the spatial distribution of ECC (72%) and LCC (28%) in Kraichgau

^b LAI data for maize in 2013 were not measured

^c Since LAI data for maize in 2013 were not available, LAI dynamics were derived from the field data of 2009-2012 for maize in the Kraichgau region

188

189

190 **2.3 Simulation runs**

191 We firstly quantified the extent to which ECC and LCC differ with regard to their energy and water
 192 fluxes, surface (TS) and soil temperature (TG). For this, we performed one simulation for each
 193 crop group using the mean LAI and the mean GVF dynamics observed during the two growing
 194 seasons (see Table 2 and Table 3).

195



196 Secondly, to determine the effect of splitting up the vegetation dynamics of a generic crop into
197 that of ECC and LCC, we compared the following two simulation runs:

198 Run 1: Noah-MP was forced with the GVF and LAI dynamics of the generic crop (Table 2 and
199 Table 3). Accordingly, in this simulation, we first computed the weighted mean of the vegetation
200 properties (GVF and LAI), and subsequently simulated the surface energy fluxes, TS and TG.

201 Run 2: We first simulated the energy and water fluxes for ECC and LCC with their crop-specific
202 vegetation dynamics, and then used the weighted mean of the two simulations of fluxes and
203 temperatures.

204

205 Thirdly, we studied the effect of increasing the LCC share on the surface energy fluxes, surface
206 and soil temperatures. As mentioned in the Introduction, the maize cropping area in Germany
207 increased by 53% over the last decade. In our study region, this increase corresponds to a rise of
208 the LCC share from 28% to 38%. To study the effect of this land use change on the Noah-MP
209 simulations, we performed one additional generic crop simulation, but this time the generic crop
210 dynamics was computed with a LCC share of 38%.

211

212 **3 Results**

213 **3.1 ECC vs. LCC**

214 Over the growing season, ECC and LCC show distinct differences with regard to energy
215 partitioning at the land surface (Figure 1). The observed shifts were strongest for LE and H. Early
216 covering crops already reached their maximum LE flux in May, after which LE declined during
217 the growing season. In contrast, LCC showed a continued increase in LE over the season, peaking
218 three months later in August. The smallest difference in evapotranspiration between both crops
219 types was on average 0.4 mm day^{-1} ($\text{LE } 0.9 \text{ MJ m}^{-2}\text{day}^{-1}$) in June, while the largest mean deviation
220 of -2.3 mm day^{-1} ($\text{LE } -5.7 \text{ MJ m}^{-2}\text{day}^{-1}$) occurred in August (Table 4). With regard to the H flux,
221 the situation was opposite (Figure 1). In the case of ECC, H flux increased continuously over the
222 course of the growing season, peaking in August. In contrast, LCC already reached the H
223 maximum in May. Afterwards, H decreased continuously until late August. As for LE, the smallest
224 ($-1.2 \text{ MJ m}^{-2}\text{day}^{-1}$) and largest ($5.3 \text{ MJ m}^{-2}\text{day}^{-1}$) mean differences in H between ECC and LCC



225 were observed in June and August, respectively (Table 4). Compared with LCC, the higher latent
 226 heat fluxes of ECC in May and June resulted in a cooler land surface, on average by -2.6°C and $-$
 227 1.0°C , respectively (Table 4). From July to August the situation was reversed: because latent heat
 228 fluxes of ECC are distinctly lower than that of LCC, the surface temperature at ECC sites was up
 229 to 4°C warmer than at LCC sites (Figure 2).

230

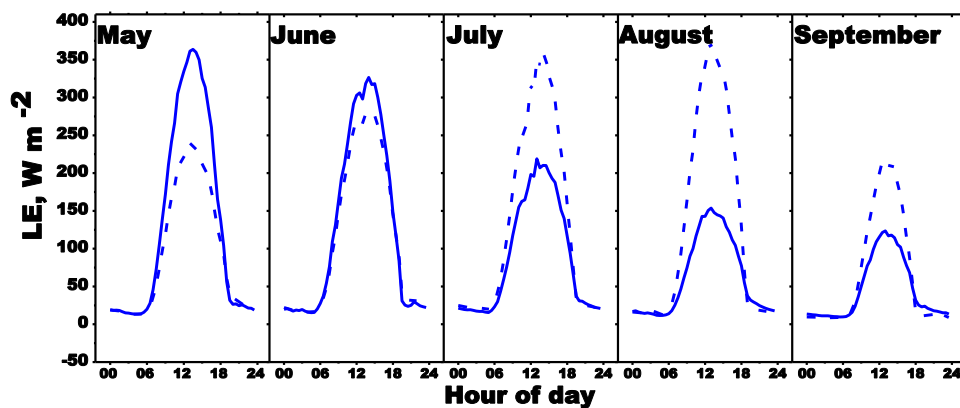
231 The mean difference in daily ground heat flux between ECC and LCC during the growing season
 232 ranged between -0.2 MJ m^{-2} and 0.2 MJ m^{-2} (Table 4). Also for the ground heat flux, the smallest
 233 difference between both crops types was observed in June (0.05 MJ m^{-2}).

234 **Table 4.** Mean differences (ECC minus LCC) in latent (LE), sensible (H) and ground heat (G) fluxes,
 235 mean surface temperature (TS) and mean ground temperature (TG) between ECC and LCC simulations.

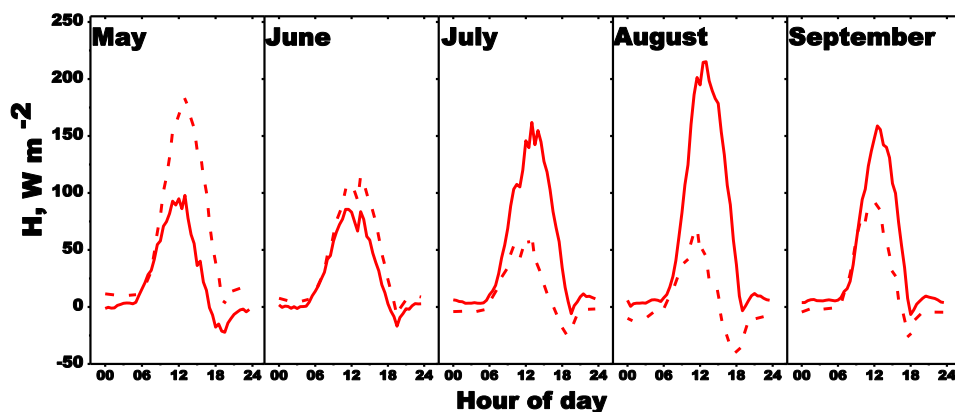
| Month | DOY | LE mm d^{-1} | $\text{MJ m}^{-2} \text{ d}^{-1}$ | H $\text{MJ m}^{-2} \text{ d}^{-1}$ | G $\text{MJ m}^{-2} \text{ d}^{-1}$ | TS $^{\circ}\text{C}$ | TG $^{\circ}\text{C}$ |
|-----------|-----------|--------------------------|-----------------------------------|--|--|--------------------------|--------------------------|
| May | 121 – 151 | 1.3 | 3.3 | -3.1 | -0.2 | -2.6 | -2.2 |
| June | 152 – 181 | 0.4 | 0.9 | -1.2 | 0.05 | -1.0 | -0.9 |
| July | 182 – 212 | -1.5 | -3.8 | 3.3 | 0.2 | 2.1 | 1.8 |
| August | 213 – 243 | -2.3 | -5.7 | 5.3 | 0.1 | 3.2 | 2.4 |
| September | 244 – 273 | -0.7 | -1.8 | 2.1 | -0.1 | 1.9 | 1.2 |

DOY - day of a year

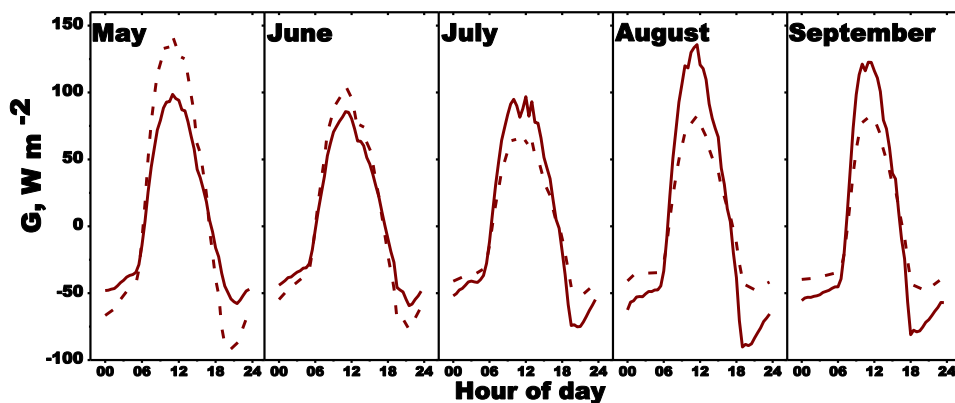
236



237



238



239

240

241

242

Figure 1. Simulation results of Noah-MP LSM for latent (LE), sensible (H) and ground heat (G) flux. Simulations were performed for two types of crops: early covering (solid line) and late covering (dashed line).

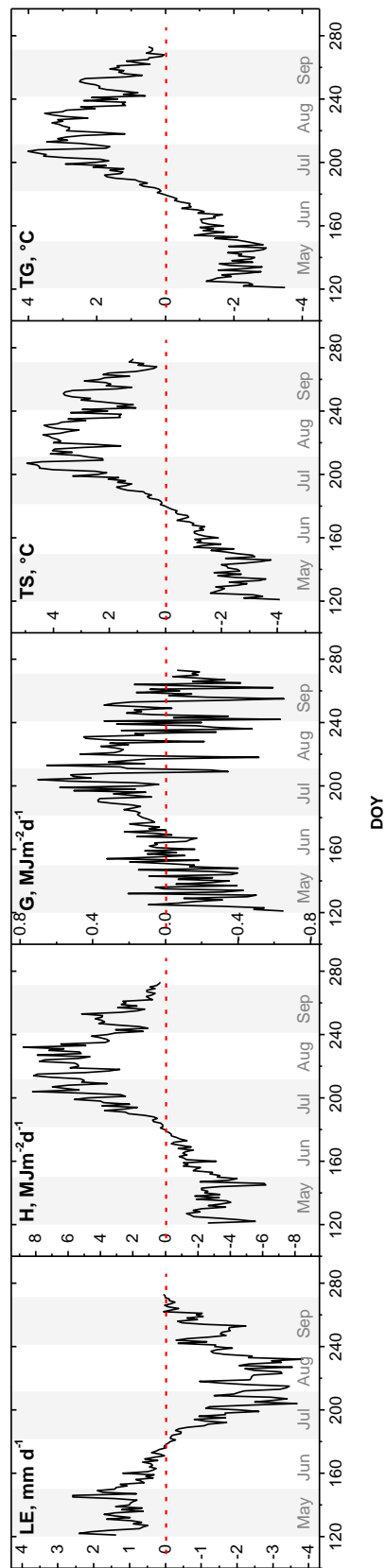


Figure 2. Differences (ECC minus LCC) in latent (LE), sensible (H) and ground heat (G) fluxes, mean surface temperature (TS) and mean ground temperature (TG) between simulations for ECC and LCC.

243
244
245
246
247

248
249
250
251
252
253



254 **3.2 Run 1 vs. Run 2 (Generic crop vs. weighted mean of ECC and LCC)**

255 The generic crop simulation run (Run 1) generally yielded higher LE fluxes than Run 2 (i.e.
 256 splitting up the generic crop into ECC and LCC) (Figure 3). During the growing season the mean
 257 difference in evapotranspiration between two runs was 0.1 mm day^{-1} (LE $3.7 \text{ MJ m}^{-2}\text{day}^{-1}$) (Table
 258 5). Smallest mean monthly differences occurred in June and September: 0.02 mm day^{-1} (LE 0.4 MJ
 259 $\text{m}^{-2}\text{day}^{-1}$) and 0.03 mm day^{-1} (LE $1 \text{ MJ m}^{-2}\text{day}^{-1}$), respectively. The most pronounced differences
 260 in LE flux were recorded in late July (DOY 197-208) (Figure 4). The average difference in half-
 261 hourly fluxes over this period, between 9 a.m. and 6 p.m, was 36 W m^{-2} , and the highest half-
 262 hourly deviation between both runs was 83 W m^{-2} (Figure 4). The highest daily deviation was 0.8
 263 mm day^{-1} (Figure 3). Over the whole season, the cumulative difference in evapotranspiration
 264 between two runs was 20 mm , leading to a 16 percent lower seasonal water balance (SWB) in Run
 265 1 (SWB: -133 mm) than in Run 2 (SWB: -113 mm).

266 **Table 5.** Mean differences in latent (LE), sensible (H) and ground heat (G) fluxes, surface
 267 temperature (TS) and ground temperature (TG) between Run 1 and Run 2 simulations. Numbers
 268 in brackets: the relative difference between Run 1 and Run 2 simulations in percentage.

| Month | DOY | LE mm d^{-1} | $\text{MJ m}^{-2} \text{d}^{-1}$ | H $\text{MJ m}^{-2} \text{d}^{-1}$ | G $\text{MJ m}^{-2} \text{d}^{-1}$ | TS $^{\circ}\text{C}$ | TG $^{\circ}\text{C}$ |
|-------------|-----------|--------------------------|----------------------------------|---------------------------------------|---------------------------------------|--------------------------|--------------------------|
| May | 121 – 151 | 0.1 (3) | 0.3 | -0.3 (19) | -0.003 (1) | -0.3 (2) | -0.02 (0.1) |
| June | 152 – 181 | 0.02 (0.4) | 0.04 | -0.1 (4) | 0.001 (1) | -0.1 (1) | 0.01 (0.05) |
| July | 182 – 212 | 0.3 (7) | 0.6 | -0.6 (21) | -0.016 (4) | -0.4 (2) | -0.1 (0.6) |
| July* | 197 – 208 | 0.5 (14) | 1.3 | -1.2 (46) | -0.034 (10) | -1.0 (4) | -0.2 (1) |
| August | 213 – 243 | 0.2 (7) | 0.5 | -0.6 (18) | 0.004 (2) | -0.3 (1) | 0.01 (0.03) |
| September | 244 – 273 | 0.03 (1) | 0.1 | -0.2 (5) | 0.005 (3) | -0.1 (1) | 0.1 (0.4) |
| Mean | | 0.1 (3.7) | 0.3 | -0.4 (13.2) | -0.002 (1) | -0.2 (1.4) | -0.01 (0.1) |

DOY - day of a year

269

270

271 In contrast, H fluxes of Run 1 were mostly lower over all months than those simulated in Run 2
 272 (Figure 3). From May to September, the mean difference in H fluxes was about -0.4 MJ m^{-2} (-
 273 13 %) (Table 5). The smallest difference occurred again in June, the largest difference again in
 274 late July (Figure 4). During DOY 197-208 the mean differences in half hourly H fluxes was about
 275 -29 W m^{-2} , the peak deviation being -72 W m^{-2} (9 a.m.-6 p.m) (Figure 4). Cumulating these



276 differences over the day reduced the production of sensible heat on average in the order of
277 1.2 MJ m^{-2} , corresponding to a 46 %reduction compared to Run 2 (Table 5). Ground heat fluxes
278 as well as soil temperature were affected only moderately by the different vegetation
279 parameterization of Run 1 and 2 (Figure 4, Figure 3). As for LE and H, the largest mean differences
280 in G fluxes were observed during DOY 197-208 ($-0.034 \text{ MJ m}^{-2} = 10\%$) (Table 5).

281

282 Due to the humid bias of Run 1, the canopy surface was cooler than in Run 2 in all months. On
283 average, TS of Run 1 was $0.2 \text{ }^{\circ}\text{C}$ ($\sim 1.4\%$) lower during the growing season than in Run 2. In late
284 July (DOY 197-208) the mean daily difference was $-1 \text{ }^{\circ}\text{C}$ (Table 5, Figure 3) and reached a daytime
285 (9a.m.-6p.m.) peak difference of up to $-2.6 \text{ }^{\circ}\text{C}$ (Figure 4).

286

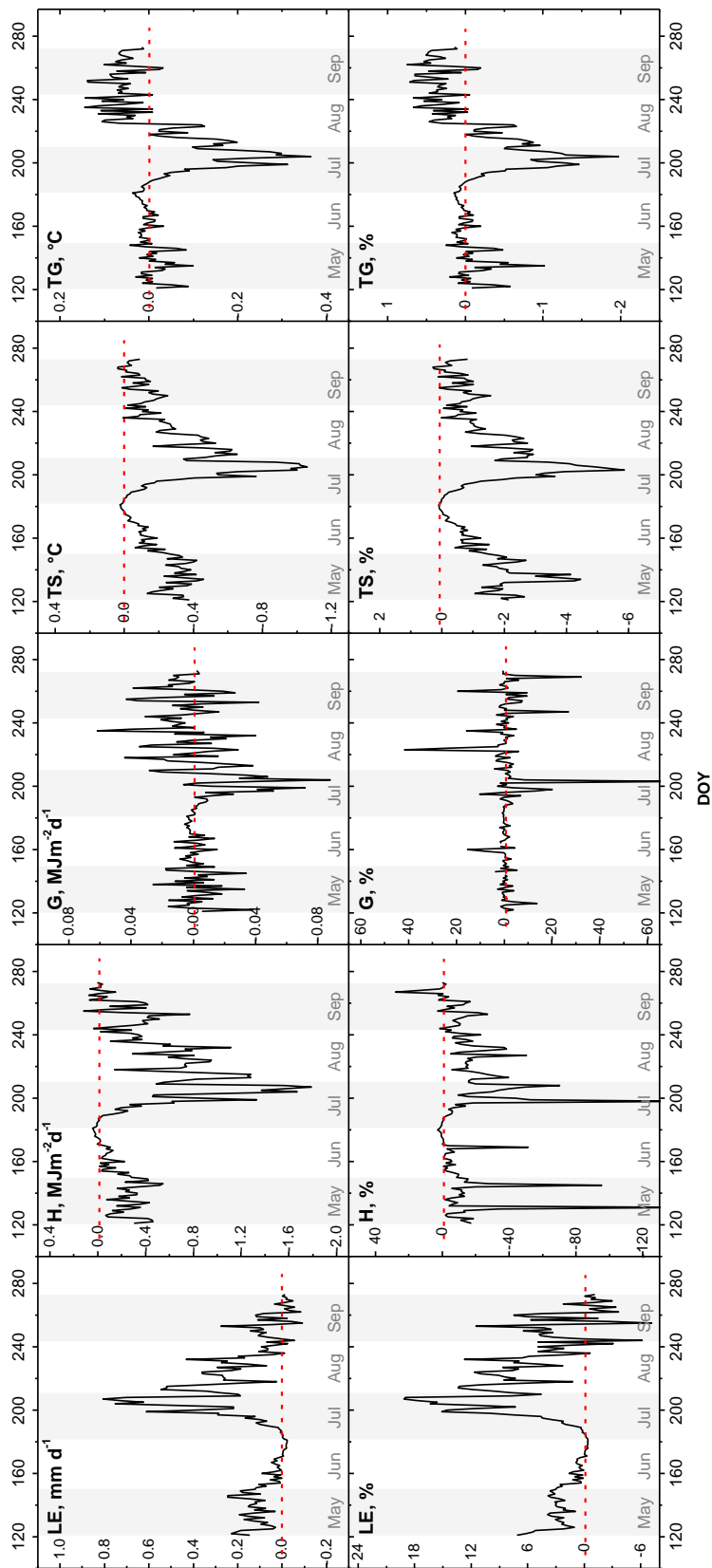


Figure 3. Differences in latent (LE), sensible (H) and ground heat (G) fluxes, mean surface temperature (TS) and mean ground temperature (TG) between Run 1 and Run 2 simulations (*Run 1 - Run 2*). Given percentages are relative differences between Run 1 and Run 2 simulations.

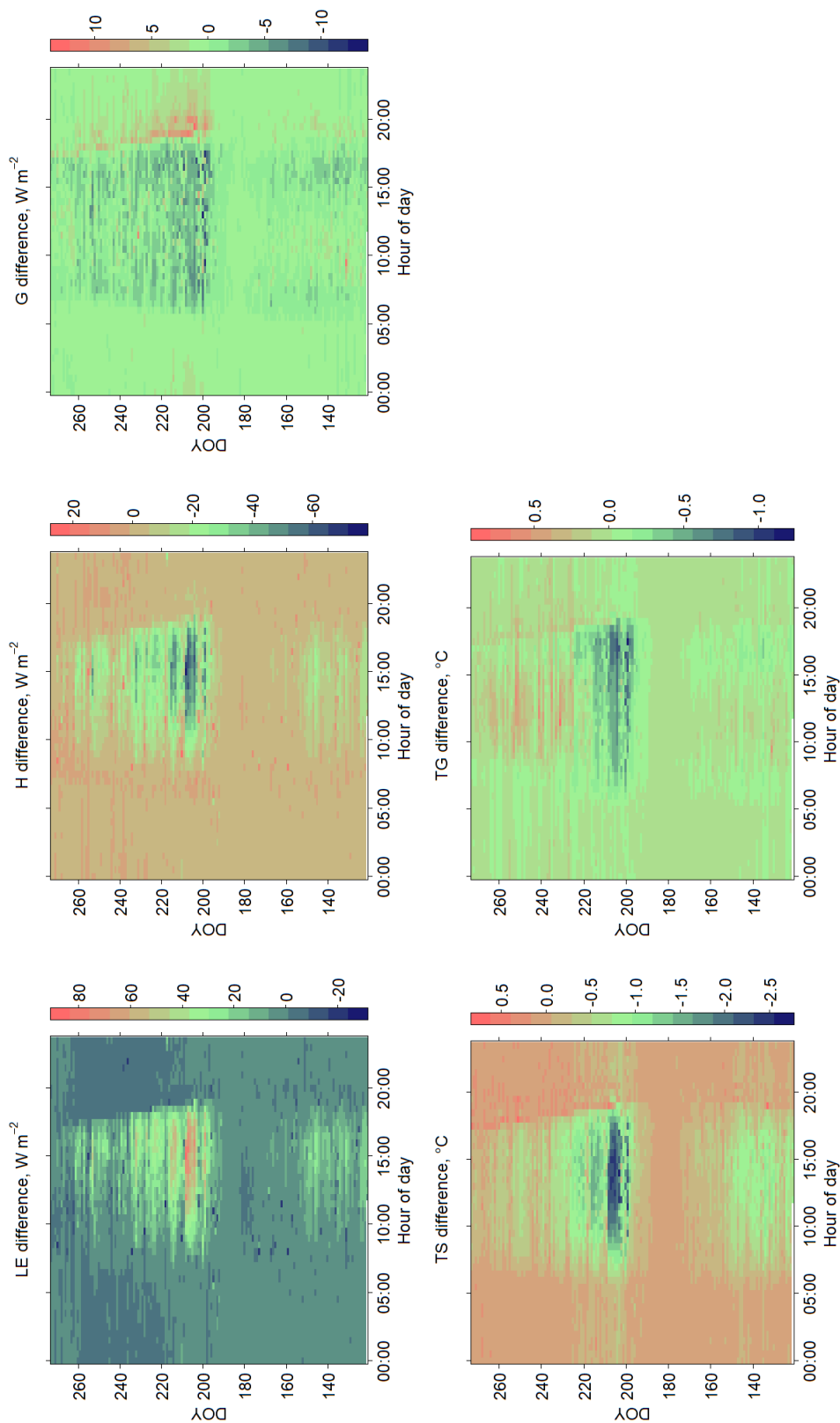


Figure 4. Differences in latent (LE) and ground heat (G) fluxes, mean surface temperature (TS) and mean ground temperature (TG) between Run 1 (generic crop) and Run 2 (weighted mean of early and late covering crops) simulations (*Run 1 - Run 2*).



292 3.3 Land use change towards LCC

293 Increasing the LCC fraction from 28% to 38% mainly led to changes in LE and H fluxes (Table
 294 6). That LCC increase lowered the LE flux ($-0.3 \text{ MJ m}^{-2} \text{ day}^{-1}$ -or $\text{ET } 0.1 \text{ mm day}^{-1}$) early in the
 295 season. This was accompanied by a higher H flux ($+0.3 \text{ MJ m}^{-2} \text{ day}^{-1}$), which in turn led to a 0.3
 296 °C warmer surface temperature than for the runs with the actual ECC-LCC ratio. From July to
 297 September, increasing the LCC fraction boosted evapotranspiration by about 0.2 mm day^{-1} (LE
 298 $0.4 \text{ MJ m}^{-2} \text{ day}^{-1}$) and decreased the H flux by about $0.3 \text{ MJ m}^{-2} \text{ day}^{-1}$ (Table 6). The largest half-
 299 hourly differences occurred in August (DOY 213-243, Figure 5), amounting to $+40 \text{ W m}^{-2}$
 300 and -30 W m^{-2} for LE and H, respectively. The smallest deviations for both fluxes were recorded
 301 in June. Over the July–September period, the higher LE flux of the simulation run with the
 302 increased LCC fraction cooled the land surface up to -1 °C (Figure 5). In general over the growing
 303 season, increasing the LCC share by 10% led to an increase in cumulative evapotranspiration,
 304 which in turn resulted in a 10 mm lower seasonal water balance (SWB: -143 mm).

305

306 With regard to the ground heat flux, increasing the LCC fraction led to an up to 10 W m^{-2} higher
 307 flux over the noon time during the second part of the growing season (Figure 5), whereas early in
 308 the season the differences did not exceed 0.2 °C (Table 6).

309 **Table 6.** Mean differences in latent (LE), sensible (H) and ground heat (G) fluxes, surface temperature
 310 (TS) and ground temperature (TG) between simulations with the LCC fraction increased by 10 % and the
 311 baseline simulation (*increased LCC share minus baseline simulation*). Numbers in brackets: the relative
 312 difference between *increased LCC share and baseline simulation* in percentage

| Month | DOY | LE mm d^{-1} | MJ $\text{m}^{-2}\text{d}^{-1}$ | H $\text{MJ m}^{-2}\text{d}^{-1}$ | G $\text{MJ m}^{-2}\text{d}^{-1}$ | TS $^{\circ}\text{C}$ | TG $^{\circ}\text{C}$ |
|-----------|-----------|--------------------------|---------------------------------|--------------------------------------|--------------------------------------|--------------------------|--------------------------|
| May | 121 - 151 | -0.1 (3.3) | -0.3 | 0.3 (14) | 0.02 (1) | 0.3 (2) | 0.2 (1) |
| June | 152 - 181 | -0.04 (1.0) | -0.1 | 0.1 (6) | -0.005 (0.5) | 0.1 (1) | 0.1 (1) |
| July | 182 - 212 | 0.2 (4.3) | 0.4 | -0.3 (12) | -0.02 (6) | -0.2 (1) | -0.2 (1) |
| August | 213 - 243 | 0.2 (7.6) | 0.6 | -0.5 (17) | -0.01 (1) | -0.3 (2) | -0.2 (1) |
| September | 244 - 273 | 0.1 (3.8) | 0.2 | -0.2 (4) | 0.01 (4) | -0.2 (1) | -0.1 (1) |

DOY - day of a year

313

314

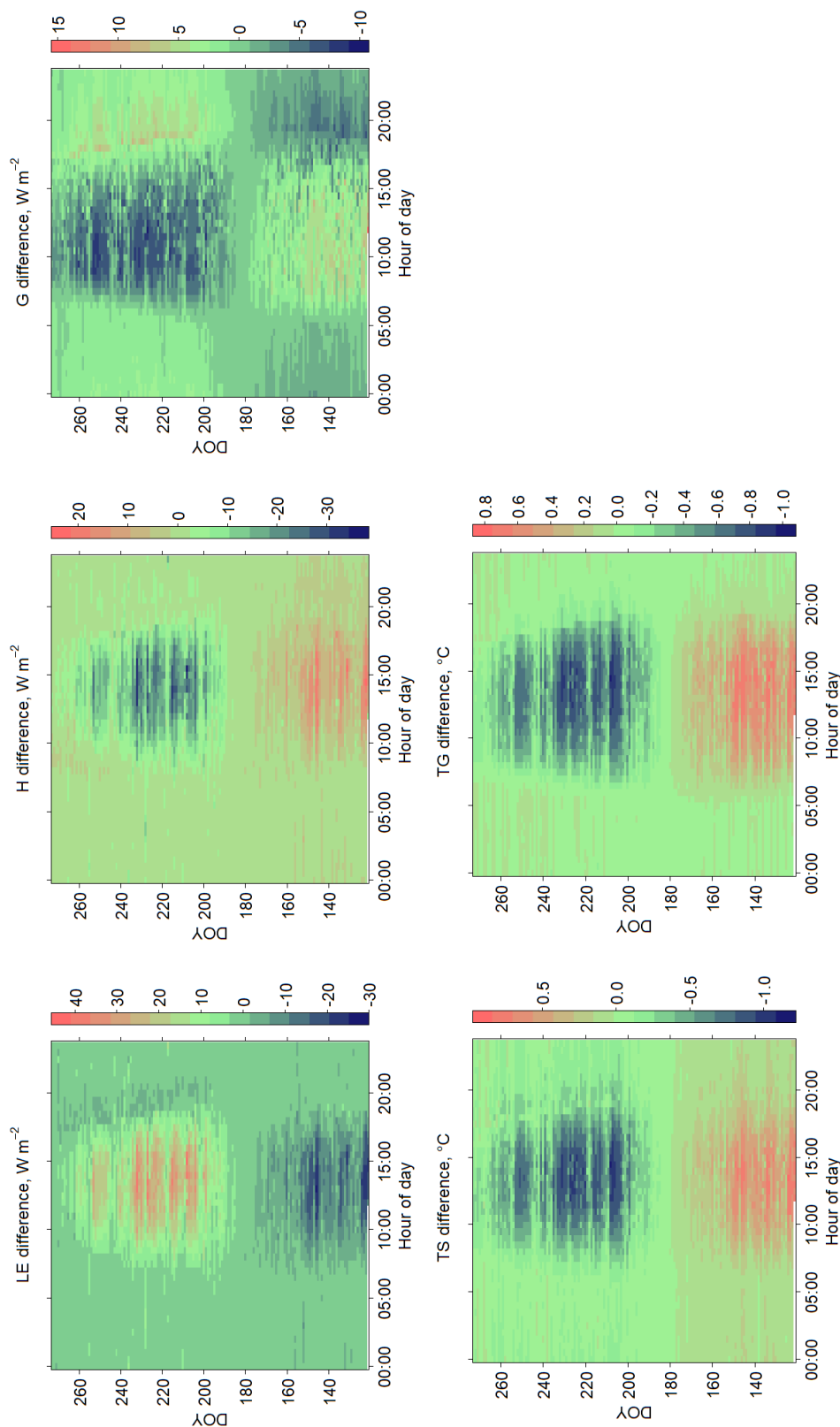


Figure 5. Impact of increasing the LCC fraction from 28% to 38% on latent (LE), sensible (H) and ground heat (G) fluxes, surface temperature (TS) and ground temperature (TG) (*Increased LCC share minus baseline simulation*).



316 **4 Discussion**

317 The comparison of the ECC and LCC simulations confirmed that GVF and LAI significantly affect
318 the partitioning of surface energy fluxes. LE flux increases with crop growth and peaks when the
319 canopy is fully developed, i.e. have maximum LAI and GVF. By contrast, the highest H and G
320 fluxes were observed at sparsely covered fields or on the fields with a senescent canopy. During
321 the main growth period of crops, H and G fluxes were quite low. ECC and LCC crops vary
322 significantly in sowing and harvest date, leaf area and senescence dynamics, water use efficiency
323 and phenology. Their surface energy fluxes therefore differ distinctly. Our simulation results are
324 in agreement with experimental data of Wizeman et al. (2014) as well as with modeling studies of
325 Sulis et al. (2015), Tsvetsinskaya et al. (2001b), Xue et al. (1996) or Ingwersen et al. (2018).

326

327 The potential increase of the LCC fraction (driven by the high demand for biogas and forage
328 production) leads to significant changes in the partitioning of the energy fluxes at the croplands.
329 In recent years the total area under maize in Germany has more than doubled. This corresponds to
330 an approximately 10% increase of the LCC fraction for the study region. In the early vegetation
331 period, the altered ECC-LCC ratio leads to a decrease of evapotranspiration, an increase of H
332 fluxes, and a warmer cropland surface because, during that period, a higher fraction of fields is
333 bare or sparsely covered with vegetation. In mid-June, the situation reverses. The higher share of
334 LCC boosts LE fluxes, decreases H fluxes and lowers surface temperatures. The increased
335 evapotranspiration over the growing season, in turn, leads to a lower seasonal water balance.

336

337 Comparing the generic crop simulation (Run 1) with the weighted mean of two separate
338 simulations for ECC and LCC (Run 2) showed the largest difference over the second half of the
339 growing season, particularly during late July/early August. In July, ECC become senescent: GVF
340 drops sharply and green LAI equals zero. In early August, ECC are usually harvested. In contrast,
341 LCC have a developed ground-covering canopy during July-August. Leaves of these crops are still
342 green in September. This transition period is very smooth in the case of the generic crop, resulting
343 on average in about 14 % higher LE and in about 46%, 10% and 4% lower H, G and surface
344 temperature, respectively, compared with Run 2.

345

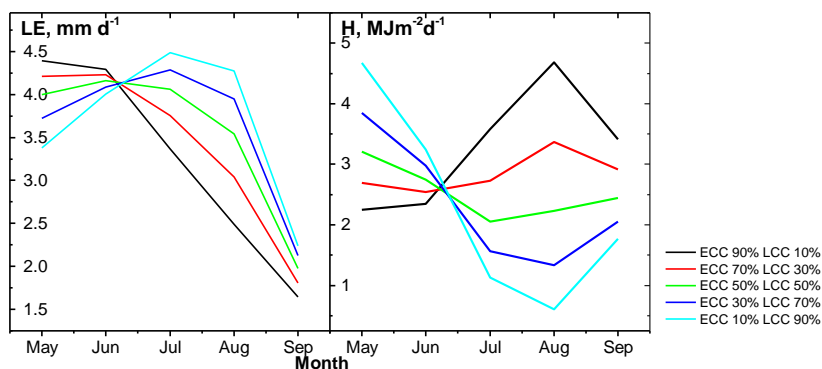


346 The results presented above apply to the ECC-LCC ratio within our study area. What can we expect
347 in agricultural landscapes with different ECC-LCC ratios? The ECC-LCC ratio has nearly no effect
348 on energy partitioning in June, whereas in May, July and August its influence on the turbulent
349 fluxes is pronounced (Figure 6). The weak effect in June is because, during this period, the LAI
350 and GVF of ECC and LCC are similar (Figure 8). In the other months, however, the ECC-LCC
351 ratio heavily affects the energy partitioning. For example, increasing the LCC share from 10% to
352 90% boosts daily evapotranspiration in August from 2.5 mm d^{-1} to 4.3 mm d^{-1} , decreases the H
353 flux by about $4.1 \text{ MJ m}^{-2} \text{ d}^{-1}$ and cools down the cropland surface by $2 \text{ }^{\circ}\text{C}$. Over the growing season,
354 the increase in the LCC share leads to a general increase in evapotranspiration, which in turn
355 lowers the seasonal water balance (Table 7). Moreover, different ECC-LCC ratios will also affect
356 the above-mentioned humid bias of the generic crop parameterization (Figure 7). The bias is largest
357 if ECC and LCC shares are balanced (ECC 50% and LCC 50 %), whereas combinations with one
358 predominant crop distinctly lower the bias. In August, for instance, the LE differences between the
359 two runs with ECC 50%- LCC 50% equal 0.27 mm day^{-1} , while ECC 10%- LCC 90 % yields
360 differences of 0.09 mm day^{-1} .

361 **Table 7.** Weather data and simulation results of Noah-MP LSM for cumulative evapotranspiration for the
362 Kraichgau region. Simulations were performed considering different shares of early covering crops
363 (ECC) and late covering crops (LCC).

| ECC and LCC shares | Total rainfall (R), mm | Cumulative evapotranspiration (ET), mm | Seasonal water balance (R-ET), mm |
|--------------------|------------------------|--|-----------------------------------|
| ECC 90% LCC 10% | 388 | 496 | -108 |
| ECC 70% LCC 30% | 388 | 522 | -134 |
| ECC 50% LCC 50% | 388 | 544 | -156 |
| ECC 30% LCC 70% | 388 | 557 | -169 |
| ECC 10% LCC 90% | 388 | 563 | -175 |

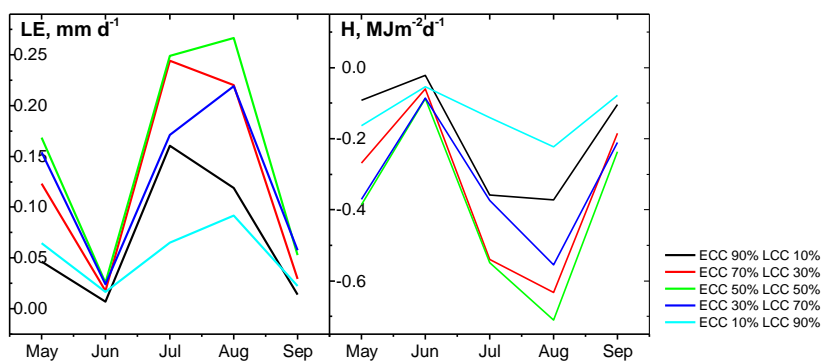
364



365

366 **Figure 6.** Simulation results of Noah-MP LSM for latent (LE) and sensible (H) heat flux. Simulations
367 were performed considering different shares of ECC and LCC.

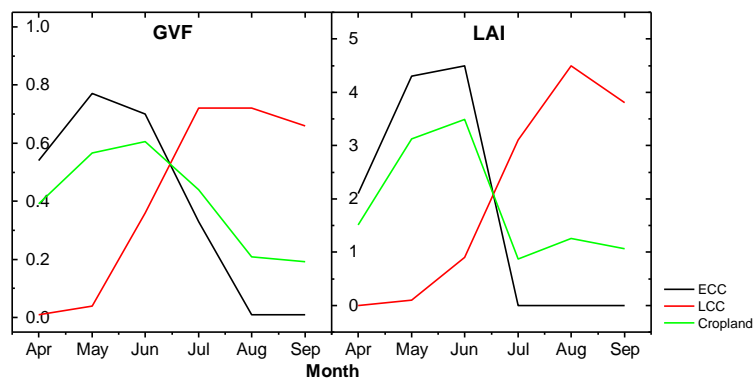
368



369

370 **Figure 7.** Differences in latent (LE) and sensible heat (H) fluxes between Run 1 and Run 2 simulations
371 (*Run 1 - Run 2*). Simulations were performed considering different shares of ECC and LCC.

372



373

374 **Figure 8.** GVF and LAI dynamics of early covering crops (ECC), late covering crops (LCC) and
375 Cropland.

376



377 Our results show that performing simulations based on single dynamics for each type of crop (ECC
378 and LCC) improve simulations of surface fluxes during transition periods and at the end of the
379 growing season. Lumping ECC and LCC into one land-use class (Croplands and Pasture), as done
380 in Noah-MP, is an oversimplification. Several authors demonstrated the necessity to distinguish
381 biophysical plant parameters between substantially different crops to obtain representative
382 simulation results in the lower atmosphere (Sulis et al. 2015, Tsvetsinskaya et al. 2001b, Xue et
383 al. 1996). They showed that high-resolution spatial information on various croplands and
384 associated physiological characterizations can significantly improve the simulations of land
385 surface energy fluxes, leading to better weather and climate predictions.

386

387 Changes of LAI and GVF with plant growth lead to changes in surface albedo, bulk canopy
388 conductance and roughness length, which in turn alter the partitioning of surface energy fluxes
389 (Chen and Xie 2011, Chen and Xie 2012, Crawford et al. 2001, Tsvetsinskaya et al. 2001a, Xue et
390 al. 1996). Such altered energy partitioning at the land surface then changes the thermodynamic
391 state of the atmospheric boundary layer with regard to air temperature, surface vapor pressure,
392 relative humidity and finally rainfall (Chen and Xie 2012, McPherson and Stensrud 2005, Sulis et
393 al. 2015, Tsvetsinskaya et al. 2001b). The observed differences between Run 1 and crop-type-
394 based runs will most probably influence the simulated processes in the ABL. For instance, Sulis
395 et al. (2015) significantly improved the simulations of land surface energy fluxes by using the
396 crop-specific physiological characteristics of the plant. They observed a difference of about 40%
397 between simulated fluxes using the generic and crop-specific parameter sets. The differences in
398 the land surface energy partitioning led to different heat and moisture budgets of the atmospheric
399 boundary layer for the generic and specific (sugar beet and winter wheat) croplands. In the case of
400 specific croplands, particularly sugar beet, those authors observed a larger contribution of the
401 entrainment zone to the heat budget of the ABL as well as a shallower ABL.

402

403 McPherson and Stensrud (2005) examined the impact of directly substituting the tallgrass prairie
404 land use class with winter wheat on the formation of the ABL. These crops have different growing
405 seasons. In the U.S. Great Plains, native prairie tallgrass mainly grows in summer, while winter
406 wheat grows throughout winter and reaches maturity in late spring. Simulations showed a larger
407 LE and lower H over the area with the winter wheat stand in comparison with tallgrass. By 2100



408 UTC, LE ranged from 300 to 400 W m⁻² for the wheat run and from 200 to 275 W m⁻² for the
409 tallgrass run. H ranged from 25 to 125 W m⁻² for the former and from 100 to 200 W m⁻² for the
410 latter. Substituting tallgrass prairie with winter wheat boosted the atmospheric moisture near the
411 surface above- and downstream of the study area, and resulted in a shallower ABL above- and
412 downstream of this area. The shallower ABL reduced the entrainment of higher-momentum air
413 into the ABL and therefore led to weaker winds within the ABL.

414

415 Milovac et al. (2016) performed six simulations at 2 km resolution with two local and two nonlocal
416 ABL schemes combined with two LSMs (Noah and Noah-MP) to study the influence of energy
417 partitioning at the land surface on the ABL evolution on a diurnal scale. They observed that LE
418 simulated by Noah-MP was more than 50% lower than that simulated by Noah. As expected, a
419 lower LE resulted in a drier ABL. The ABL evolution and its features strongly influence the
420 initiation of convection and cloud formation as well as the location and strength of precipitation.
421 For instance, drier and higher ABL would yield a higher lifting condensation level, leading to
422 higher clouds and a higher probability of convective precipitation.

423



424 **5 Conclusions**

425 GVF and LAI significantly affect the simulation of energy partitioning, yielding pronounced
426 differences between ECC and LCC. In our study area, the use of a generic crop parameterization
427 (Croplands and Pasture in Noah-MP) resulted in a humid bias along with lower surface
428 temperatures. This humid bias will be largest in landscapes with a balanced share of ECC and
429 LCC, whereas in landscapes in which one of the two crop types predominate, the bias will be
430 weaker. We observed the strongest effects on turbulent fluxes over the second part of the season,
431 particularly in July-August. During this period, ECC are at senescence growth stage or already
432 harvested, while LCC have a fully developed ground-covering canopy. We therefore expect that
433 the observed differences will impact the simulation of processes in the ABL. Our results show that
434 splitting up croplands into ECC and LCC can improve LSMs, particularly during transition periods
435 and late in the growing season.

436

437 Increasing the LCC fraction by 10% reduces evapotranspiration and increases surface temperatures
438 over the first part of the growing season. Later in the season, this land use change leads to the
439 opposite situation: increased evapotranspiration accompanied by a slight cooling of the land
440 surface. Over the growing season, an increase of the LCC share by 10% leads to higher cumulative
441 evapotranspiration, which in turn lowers the seasonal water balance.

442



443 **6** **References**

444 Chen, F. and Xie, Z.: Effects of crop growth and development on regional climate: A case study
445 over East Asian monsoon area, *Clim. Dyn.*, 38, 2291-2305, 2012.

446 Chen, F. and Xie, Z.: Effects of crop growth and development on land surface fluxes, *Adv.*
447 *Atmos. Sci.*, 28, 927-944, 2011.

448 Crawford, T. M., Stensrud, D. J., Mora, F., Merchant, J. W. and Wetzel, P. J.: Value of
449 incorporating satellite-derived land cover data in MM5/PLACE for simulating surface
450 temperatures, *J. Hydrometeorol.*, 2, 453-468, 2001.

451 Ghilain, N. a., Arboleda, A. a., Sepulcre-Cantò, G., Batelaan, O., Ardö, J. d. and Gellens-
452 Meulenberghs, F. a.: Improving evapotranspiration in a land surface model using biophysical
453 variables derived from MSG/SEVIRI satellite, *Hydrology and Earth System Sciences*, 16, 2567-
454 2583, 2012.

455 Gutman, G. and Ignatov, A.: The derivation of the green vegetation fraction from
456 NOAA/AVHRR data for use in numerical weather prediction models, *Int. J. Remote Sens.*, 19,
457 1533-1543, 1998.

458 Huyghe, C., De Vlieghe, A., van Gils, B. and Peeters, A.: Grassland and herbivore production in
459 Europe and effects of common policies, Editions Quae: Versailles, France ISBN : 978-2-7592-
460 2157-8 ISSN : 1777-4624, 2014.

461 Imukova, K., Ingwersen, J. and Streck, T.: Determining the spatial and temporal dynamics of the
462 green vegetation fraction of croplands using high-resolution RapidEye satellite images, *Agric.*
463 *For. Meteorol.*, 206, 113-123, 2015.

464 Ingwersen, J., Imukova, K., Högy, P. and Streck, T.: On the use of the post-closure methods
465 uncertainty band to evaluate the performance of land surface models against eddy covariance
466 flux data, *Biogeosciences*, 12, 2311-2326, 2015.

467 Ingwersen, J., Steffens, K., Högy, P., Warrach-Sagi, K., Zhunusbayeva, D., Poltoradnev, M.,
468 Gäbler, R., Wizemann, H. -, Fangmeier, A., Wulfmeyer, V. and Streck, T.: Comparison of Noah
469 simulations with eddy covariance and soil water measurements at a winter wheat stand, *Agric.*
470 *For. Meteorol.*, 151, 345-355, 2011.

471 Ingwersen, J., Högy, P., Wizemann, H.D., Warrach-Sagi, K., Streck, T.: Coupling the land surface
472 model Noah-MP with the generic crop growth model Gecros: Model description, calibration and
473 validation. *Agric. Forest Meteorol.*, in print, 2018

474 Fachagentur Nachwachsende Rohstoffe e. V. Anbau und Verwendung nachwachsender Rohstoffe
475 in Deutschland. März 2019



- 476 Koster, R. D., Guo, Z., Dirmeyer, P. A., Bonan, G., Chan, E., Cox, P., Davies, H., Gordon, C. T.,
477 Kanae, S., Kowalczyk, E., Lawrence, D., Liu, P., Lu, C. -, Malyshev, S., McAvaney, B.,
478 Mitchell, K., Mocko, D., Oki, T., Oleson, K. W., Pitman, A., Sud, Y. C., Taylor, C. M.,
479 Verseghy, D., Vasic, R., Xue, Y. and Yamada, T.: GLACE: The Global Land-Atmosphere
480 Coupling Experiment. Part I: Overview, *J. Hydrometeorol.*, 7, 590-610, 2006.
- 481 Lhomme, J. - and Chehbouni, A.: Comments on dual-source vegetation-atmosphere transfer
482 models, *Agric. For. Meteorol.*, 94, 269-273, 1999.
- 483 McPherson, R. A. and Stensrud, D. J.: Influences of a winter wheat belt on the evolution of the
484 boundary layer, *Mon. Weather Rev.*, 133, 2178-2199, 2005.
- 485 Meier, U., Bleiholder, H., Buhr, L., Feller, C., Hack, H., Hess, M., Lancashire, P. D., Schnock,
486 U., Stauss, R., Van Den Boom, T., Weber, E. and Zwerger, P.: The BBCH system to coding the
487 phenological growth stages of plants-history and publications, *Journal für Kulturpflanzen*, 61,
488 41-52, 2009.
- 489 Miller, J., Barlage, M., Zeng, X., Wei, H., Mitchell, K. and Tarpley, D.: Sensitivity of the
490 NCEP/Noah land surface model to the MODIS green vegetation fraction data set, *Geophys. Res.
491 Lett.*, 33, 2006.
- 492 Niu, G. -, Yang, Z. -, Mitchell, K. E., Chen, F., Ek, M. B., Barlage, M., Kumar, A., Manning,
493 K., Niyogi, D., Rosero, E., Tewari, M. and Xia, Y.: The community Noah land surface model
494 with multiparameterization options (Noah-MP): 1. Model description and evaluation with local-
495 scale measurements, *J. Geophys. Res. D Atmos.*, 116, 2011.
- 496 Raddatz, R. L.: Evidence for the influence of agriculture on weather and climate through the
497 transformation and management of vegetation: Illustrated by examples from the Canadian
498 Prairies, *Agric. For. Meteorol.*, 142, 186-202, 2007.
- 499 Refslund, J., Dellwik, E., Hahmann, A. N., Barlage, M. J. and Boegh, E.: Development of
500 satellite green vegetation fraction time series for use in mesoscale modeling: Application to the
501 European heat wave 2006, *Theor. Appl. Climatol.*, 117, 377-392, 2014.
- 502 Rundquist, B. C.: The influence of canopy green vegetation fraction on spectral measurements
503 over native tallgrass prairie, *Remote Sens. Environ.*, 81, 129-135, 2002.
- 504 Santanello Jr., J. A., Peters-Lidard, C. D., Kennedy, A. and Kumar, S. V.: Diagnosing the nature
505 of land-atmosphere coupling: A case study of dry/wet extremes in the U.S. southern Great
506 Plains, *J. Hydrometeorol.*, 14, 3-24, 2013.
- 507 SRU Special Report: Climate Change Mitigation by Biomass, Special Report, The German
508 Advisory Council on the Environment,
509 http://www.umweltrat.de/SharedDocs/Downloads/EN/02_Special_Reports/2007_Special_Report
510 [_Climate_Change.html](http://www.umweltrat.de/SharedDocs/Downloads/EN/02_Special_Reports/2007_Special_Report), 2007.



- 511 Sulis, M., Langensiepen, M., Shrestha, P., Schickling, A., Simmer, C. and Kollet, S. J.:
512 Evaluating the influence of plant-specific physiological parameterizations on the partitioning of
513 land surface energy fluxes, *J. Hydrometeorol.*, 16, 517-533, 2015.
- 514 Tian, Y., Zou, C. Z., Mitchell, K. E., Wong, V., Kogan, F. N., Jiang, L. and Zhan, X.:
515 Improvements of numerical weather predictions using a new AVHRR green vegetation fraction
516 dataset, in: The International Society for Optical Engineering (SPIE), San Diego, CA, 12 August
517 2008 through 14 August 2008, 2008.
- 518 Tsvetsinskaya, E. A., Mearns, L. O. and Easterling, W. E.: Investigating the effect of seasonal
519 plant growth and development in three-dimensional atmospheric simulations. Part I: Simulation
520 of surface fluxes over the growing season, *J. Clim.*, 14, 692-709, 2001a.
- 521 Tsvetsinskaya, E. A., Mearns, L. O. and Easterling, W. E.: Investigating the effect of seasonal
522 plant growth and development in three-dimensional atmospheric simulations. Part II:
523 Atmospheric response to crop growth and development, *J. Clim.*, 14, 711-729, 2001b.
- 524 van Heerwaarden, C. C., de Arellano, J. V. -, Moene, A. F. and Holtslag, A. A. M.: Interactions
525 between dry-air entrainment, surface evaporation and convective boundary-layer development,
526 *Q. J. R. Meteorol. Soc.*, 135, 1277-1291, 2009.
- 527 Xue, Y., Fennessy, M. J. and Sellers, P. J.: Impact of vegetation properties on U.S. summer
528 weather prediction, *J. Geophys. Res. D Atmos.*, 101, 7419-7430, 1996.
- 529 LUBW, 2010. Landesanstalt für Umwelt, Messungen, Naturschutz Baden-Württemberg.
- 530 Milovac, J., Warrach-Sagi, K., Behrendt, A., Späth, F., Ingwersen, J., Wulfmeyer, V.:
531 Investigation of PBL schemes combining the WRF model simulations with scanning water vapor
532 differential absorption laser measurements, *J. Geophys. Res. Atmos.*, 121, 2016.
- 533 Nielsen, J. R., D. Ebba, A. N. Hahmann, and E. Boegh (2013), Representing vegetation
534 processes in hydrometeorological simulations using the WRF model, DTU Wind Energy, 128 p.
535 (Riso – PhD; No. 0016(EN)).
- 536 Margulis S. A. and Entekhabi, D.: Feedback between the Land Surface Energy Balance and
537 Atmospheric Boundary Layer Diagnosed through a Model and Its Adjoint. *J. Hydrometeorol.*, 2,
538 599–620., 2001
- 539 Wizemann, H.-D., Ingwersen, J., Högy, P., Warrach-sagi, K., Streck, T. and Wulfmeyer, V.:
540 Three year observations of water vapor and energy fluxes over agricultural crops in two regional
541 climates of Southwest Germany. *Meteorol.*, 2014